Received: 10 January 2021 | Revised: 5 April 2021 | Accepted: 7 April 2021

DOI: 10.1002/mrm.28818

FULL PAPER

Magnetic Resonance in Medicine

Vertical open-bore MRI scanners generate significantly less radiofrequency heating around implanted leads: A study of deep brain stimulation implants in 1.2T OASIS scanners versus 1.5T horizontal systems

Ehsan Kazemivalipour[1,2,3] | **Bhumi Bhusal**[1] | **Jasmine Vu**[1,4] | **Stella Lin**[1] | **Bach Thanh Nguyen**[1] | **John Kirsch**[5] | **Elizabeth Nowac**[6] | **Julie Pilitsis**[7] | **Joshua Rosenow**[8] | **Ergin Atalar**[2,3] | **Laleh Golestanirad**[1,4]

[1]Department of Radiology, Feinberg School of Medicine, Northwestern University, Chicago, Illinois, USA

[2]Department of Electrical and Electronics Engineering, Bilkent University, Ankara, Turkey

[3]National Magnetic Resonance Research Center (UMRAM), Bilkent University, Ankara, Turkey

[4]Department of Biomedical Engineering, McCormick School of Engineering, Northwestern University, Evanston, Illinois, USA

[5]A. A. Martinos Center for Biomedical Imaging, Massachusetts General Hospital, Boston, Massachusetts, USA

[6]Department of Neurosurgery, Albany Medical Center, Albany, New York, USA

[7]Illinois Bone and Joint Institute (IBJI), Wilmette, Illinois, USA

[8]Department of Neurological Surgery, Feinberg School of Medicine, Northwestern University, Chicago, Illinois, USA

Correspondence
Laleh Golestanirad, Department of Radiology, Feinberg School of Medicine, Northwestern University, 737 N Michigan Ave, Suite 1600, Chicago, IL 60611, USA.
Email: Laleh.rad1@northwestern.edu

Funding information
National Institutes of Health, Grant/Award Number: R03EB025344; Hitachi Healthcare Americas

Purpose: Patients with active implants such as deep brain stimulation (DBS) devices are often denied access to MRI due to safety concerns associated with the radiofrequency (RF) heating of their electrodes. The majority of studies on RF heating of conductive implants have been performed in horizontal close-bore MRI scanners. Vertical MRI scanners which have a 90° rotated transmit coil generate fundamentally different electric and magnetic field distributions, yet very little is known about RF heating of implants in this class of scanners. We performed numerical simulations as well as phantom experiments to compare RF heating of DBS implants in a 1.2T vertical scanner (OASIS, Hitachi) compared to a 1.5T horizontal scanner (Aera, Siemens).

Methods: Simulations were performed on 90 lead models created from post-operative CT images of patients with DBS implants. Experiments were performed with wires and commercial DBS devices implanted in an anthropomorphic phantom.

Results: We found significant reduction of 0.1 g-averaged specific absorption rate (30-fold, $P < 1 \times 10^{-5}$) and RF heating (9-fold, $P < .026$) in the 1.2T vertical scanner compared to the 1.5T conventional scanner.

Conclusion: Vertical MRI scanners appear to generate lower RF heating around DBS leads, providing potentially heightened safety or the flexibility to use sequences with higher power levels than on conventional systems.

Bhumi Bhusal and Ehsan Kazemivalipour contributed equally to this work.

KEYWORDS
deep brain stimulation, finite element method, medical implants, MR-guided neurosurgery, MRI safety, open-bore vertical MRI, RF heating

1 | INTRODUCTION

The rising prevalence of chronic diseases coupled with the rapidly aging population worldwide has increased the demand for medical implants. It is estimated that 50-75% of patients with active electronic implants will need MRI during their lifetime, with many patients requiring repeated examination. Advances in device engineering have led to a new generation of electronic implants that are largely immune to MRI-generated static and gradient fields. Tissue heating from the radiofrequency (RF) excitation field, however, remains a major issue. This *"antenna effect"*[1,2] happens when the electric field of the MRI transmit coil couples with implanted leads, causing the specific absorption rate (SAR) of the RF energy to significantly amplify in the tissue around the implant's tip. Given the potential for fatal hazards, the conditions under which patients with conductive implants are indicated for MRI are highly restrictive. In most patients with DBS devices, for example, MRI is only allowed at 1.5T field strength, using pulse sequences with a SAR of 0.1 W/kg (30 times below the Food and Drug Administration [FDA] limit for scanning in the absence of implants) or B_1rms < 2 μT.[3] There are serious drawbacks due to these restrictions as MRI protocols that optimally visualize DBS targets and electrodes have much higher SAR than current recommendations allow. Adjusting imaging parameters (eg, increasing repetition time [TR] or reducing the flip angle [FA]) is not enough to make them compliant.[4-6]

To date, the majority of MRI safety studies that aimed to quantify RF heating of DBS implants have been performed in horizontal closed-bore MRI scanners. Vertical scanners, originally introduced as low-field open-bore systems, are now available at high field strength (eg, 1.2T) capable of high-resolution structural and functional studies. These systems have a 90° rotated RF coil and, thus, generate a fundamentally different distribution of electric and magnetic fields inside the body. As the orientation and phase of MRI incident electric field along the trajectory of an elongated implant has a substantial effect on its RF heating,[7-10] vertical scanners can theoretically generate significantly different RF heating compared to their conventional counterparts.

In a preliminary simulation study with three simplified DBS lead models, we showed that a vertical butterfly coil generated 4- to 14-fold lower SAR at tips of implanted leads compared to a horizontal birdcage coil.[11] Later, we extended the study to include 40 lead models based on images of patients with lead-only DBS systems which confirmed a significant reduction in RF heating.[12] Here, we report results of an expanded study on 90 patient-derived DBS lead models including both lead-only and fully implanted systems. New patients were recruited from a second DBS center to account for the surgeon-dependent variability in routing of DBS leads. The effect of the patient′s body position within the coil was examined by performing simulations RF coils at head and chest imaging landmarks. Additionally, we investigated the differential effect of RF coil's resonance frequency and field polarization on RF heating phenomenology. Finally, we conducted experiments with a commercial DBS device implanted in an anthropomorphic phantom, scanned in a 1.5T Siemens Aera scanner and a 1.2T OASIS system to compare RF heating.

2 | METHODS

2.1 | Simulations

2.1.1 | RF coils

The necessity of including geometrical details of MRI RF coils to predict MRI-induced SAR in the tissue accurately is established by pioneering works of Ibrahim et al[13,14] and Collins et al.[15,16] The so-called specific models replicate the number and position of the input excitation in the real physical coil by the presence of lumped elements (ie, resistors and capacitors), allowing to reproduce the forward and reflected power to correctly replicate electromagnetic (EM) coupling between the coil and its load.[14,17,18] We constructed numerical models of a high-pass radial planar birdcage coil[19] made of 12 vertical rungs tuned to 50.4 MHz (1.2T proton imaging) and a 16-rung high-pass birdcage coil tuned to 64 MHz (1.5T proton imaging). The vertical coil model was based on the commercial body coil in the Oasis Hitachi scanner described in Ochi et al[20] and implemented in our previous work.[11] The horizontal coil was modeled using dimensions similar to those reported in the literature.[21] Figure 1 shows the geometrical details of both coil models and their respective $\mathbf{B}_1^+$ and $\mathbf{E}$ field distribution within a human body model with no implant. The vertical coil was driven by four feeding ports arranged in the upper and lower segments, based on the information provided by the manufacturer. The horizontal birdcage was fed with two ports that were 90° apart in both position and signal phase, located at the bottom end ring. Both coils were driven in the quadrature excitation mode by

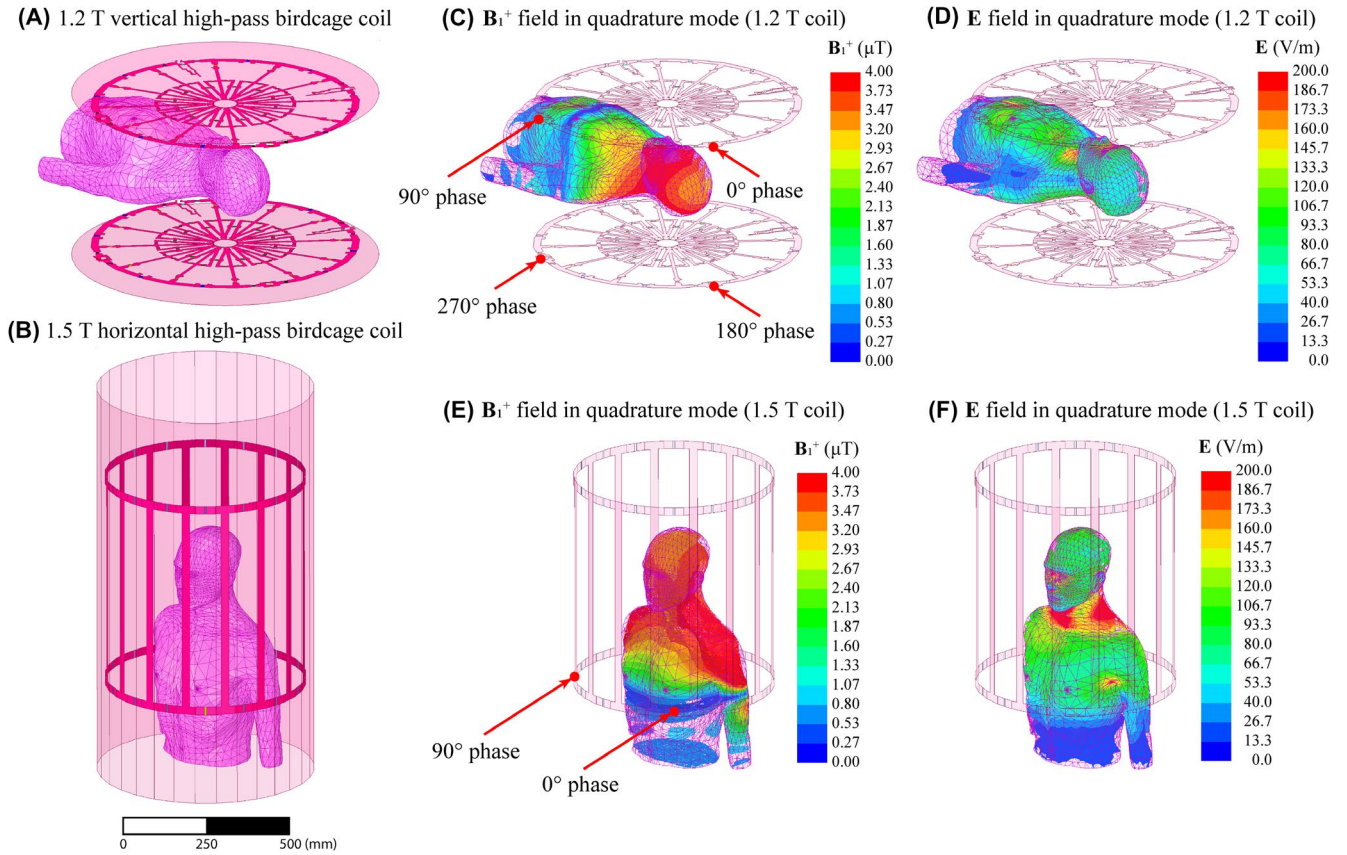

FIGURE 1 Geometry of 1.2T high-pass radial planar birdcage coil (A) and 1.5T high-pass birdcage coil (B). B_1^+ and E field distributions of 1.2T vertical coil (C,D) and 1.5T horizontal coil (E,F) within a human body model with no implants. The input power of the coils is adjusted to generate a mean $B_1^+ = 4\mu T$ on a circular axial plane passing through coil's iso-center

feeding their ports with the same amplitudes but different phases, as shown in Figure.1.

Regarding RF heating of implanted leads, there are two contributing factors that are distinctly different between the two coils: First, they have B_1-field polarization in orthogonal directions, which in turn generates different distribution of incident electric fields along lead trajectories. Second, they have different resonance frequencies (64 MHz vs. 50.4 MHz) which translates to a ~14 cm difference in RF field's wavelength in a human body model with relative permittivity of $\varepsilon_r = 80$. As RF heating is a resonance phenomenon highly sensitive to implant's electric length,[22] this frequency shift can substantially alter RF heating. To distinguish the effects of frequency from field orientation on the RF heating, we also simulated the SAR generated by a horizontal birdcage coil with the same physical dimensions as the 1.5T birdcage coil but tuned to 50.4 MHz for comparison.

2.1.2 | Patient-derived DBS lead models

RF heating of an elongated implant exquisitely depends on its trajectory,[8,23-25] and DBS leads are known to have highly variable trajectories depending on surgeon's practice style.[10] For this reason, simulations should ideally include patient-derived models that reflect inter-surgeon variability. DBS surgery is typically performed in two stages. First, electrodes are implanted in the target nucleus (eg, subthalamic nucleus [STN]) and the extracranial portion of the lead is tucked under the scalp for later connection to the implanted pulse generator (IPG). MRI in lead-only systems is useful for electrode localization. In a subsequent surgery, the IPG is implanted and leads are connected to it via subcutaneous extensions. fMRI studies that seek to disclose neuro-modulatory effects of DBS are performed on fully implanted systems. We simulated 90 unique lead models with realistic trajectories extracted from postoperative computed tomography (CT) images of 53 patients with both lead-only and fully implanted DBS systems operated at two DBS centers (Northwestern Memorial Hospital [NMH] and Albany Medical Center [AMC]) and by two neurosurgeons (J.P. and J.R.). Use of imaging data for the purpose of simulation and modeling was approved by NMH and AMC's ethics review boards.

Models of implanted leads were reconstructed following an approach for image segmentation and 3D model construction similar to our previous works.[26,27] Briefly, DBS leads

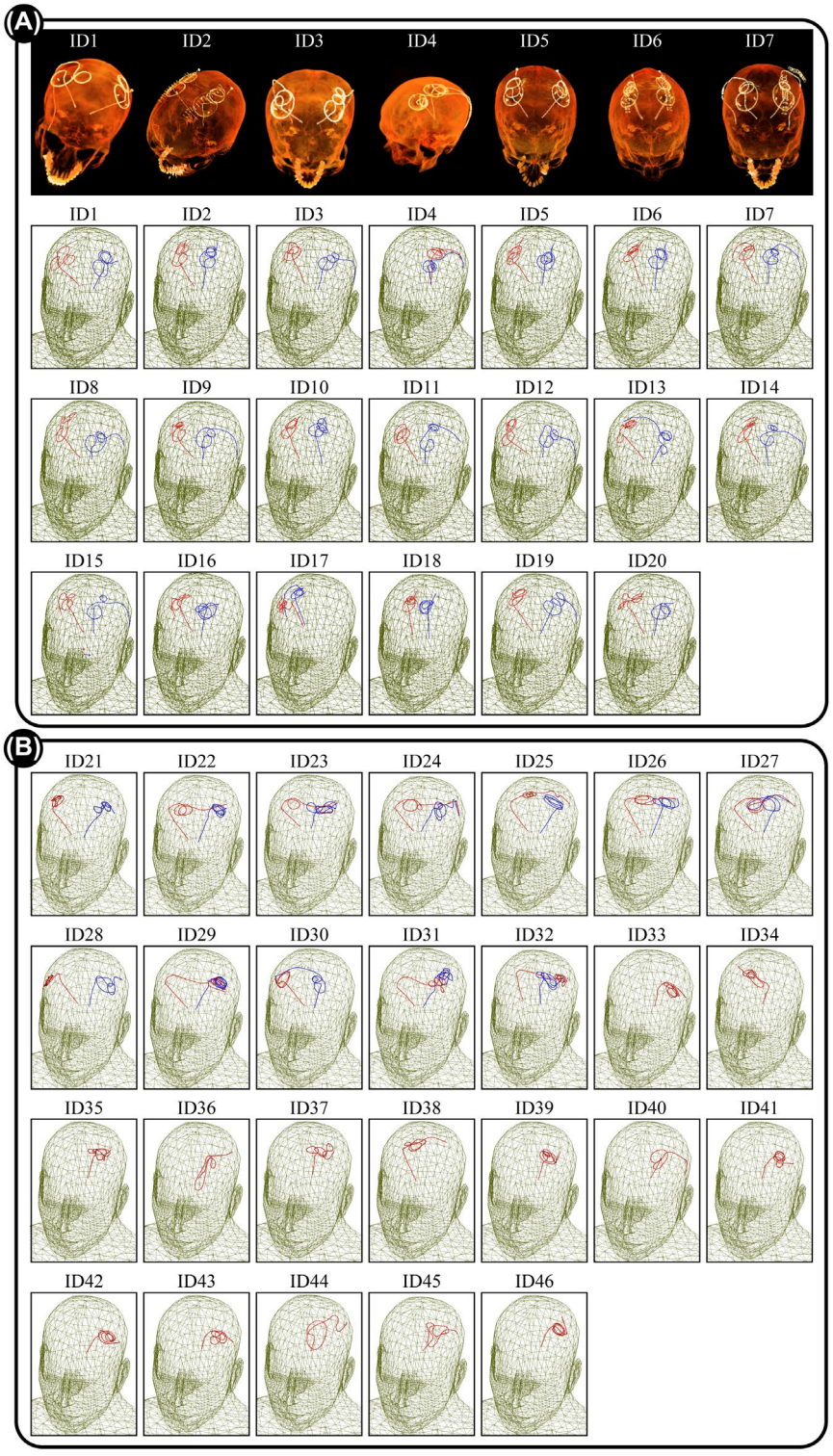

FIGURE 2 Reconstructed models of simplified DBS leads registered in a homogenous head and torso body model. A, The first 20 models are based on images of patients with bilateral lead-only systems operated for DBS surgery at Northwestern Memorial Hospital. Examples of postoperative CT images of patients (ID1-ID7) with bilateral lead-only DBS systems are also shown. B, Twenty-six models are based on images of patients with unilateral and bilateral lead only DBS systems operated for DBS surgery at Albany Medical Center

were identified in postoperative CT images using 3D Slicer 4.10.2 (http://slicer.org) visualization software and preliminary 3D surfaces were constructed. A triangulated surface model of the patient's head was also created from CT images and manually aligned to a standard homogeneous body model ($\sigma = 0.47$ S/m, $\varepsilon_r = 80$) via rigid transformation/registration (translation and rotation only, 6 degrees of freedom). The same transformation was then applied to lead trajectories to allow for anatomically representative positioning of the leads in the homogeneous body model.

From the 90 lead models, 40 models were based on images of patients with bilateral lead-only systems operated at NMH (Figure 2A) and 38 models were based on images of patients with both unilateral and bilateral lead-only systems operated at AMC (Figure 2B). Leads were modeled as a solid straight platinum-iridium (Pt:Ir) wire (diameter = 0.5 mm, σ =

4×10^6 S/m) embedded in a urethane insulation (diameter = 1 mm, $\varepsilon_r = 3.5$) with a 2 mm exposed tip. Additionally, we simulated 12 models of fully implanted devices (lead + extension + IPG) based on imaging data from 7 patients operated at AMC (Figure 3). For patients with fully implanted systems, a homogenous body model was directly created from head and neck CT images of the patient; thus, no additional alignment was necessary to position the device.

2.1.3 | Imaging landmarks

RF heating of a conductive implant depends on the distribution of MRI electric fields inside the body and around the implant, which varies by changing the position of the body inside the RF coil.[21,28,29] To investigate the effect of imaging landmark, we performed simulations with the body model positioned either with the head or chest at the coil's iso-center, corresponding to neuroimaging and cardiac imaging, respectively (Figure 4).

2.1.4 | Field calculations and numerical convergence

All simulations were implemented in ANSYS Electronics Desktop 19.2, on a Dell PowerEdge R740xd system with 1.5TB RAM and two Intel(R) Xenon(R) Gold 6140 CPUs (2.3 GHz, 36 cores). For each simulation, the input power of both coils was adjusted to produce a mean $B_1^+ = 4\mu T$ over an axial circular plane (diameter = 48 mm) positioned inside the body model and passing through the coil's iso-center. HFSS built-in SAR calculator module, which implements the IEEE STD P1528.4 recommendation, was used to calculate the maximum of 0.1 g-averaged SAR (0.1 g-SAR_{max}) inside a cubic volume of $20 \times 20 \times 20$ mm^3 surrounding the tip of the lead, labeled as SAR box.

The initial mesh was set such that the maximum element size was <5 mm for the RF coils, <1 mm on the lumped ports, and <25 mm on coil's RF shields. Within the body volume, the mesh size was restricted to be <35 mm, with the exception of the cubic volumes (SAR boxes) surrounding implant tips which enforced a mesh element length of <1 mm. Mesh size on the surface of lead wires and their insulations were set to be <0.5 mm. ANSYS HFSS follows an adaptive mesh scheme with successive refinement of an initial mesh between iterative passes. At each adaptive pass, scattering parameters (S-parameters) are evaluated at each port and compared to the previous pass. Simulations were considered to be converged when the change in the magnitude of the S-parameters between two consecutive passes fell below a set threshold of 0.03. Satisfying this convergence criterion on S-parameters is shown to also guarantee the convergence of local power deposited in the tissue around implanted leads (calculated as $\frac{\sigma|E|^2}{\rho}$).[30] All simulations converged with two to four adaptive passes. Examples of mesh distributions in the SAR box, lead, insulation, and IPG as well as distribution of 0.1 g-SAR for a patient with bilateral lead has been shown in Figure 5. Supporting Information Table S1, which is available online, provides more information on convergence assessment by directly monitoring iterative SAR values instead

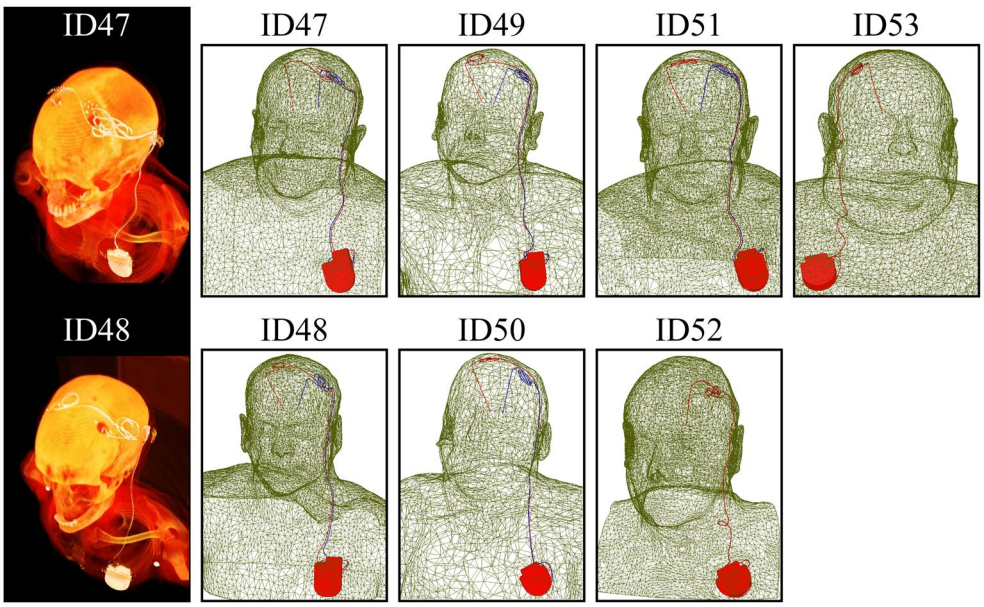

FIGURE 3 Patient-specific models of full DBS systems. The models are based on post-operation CT images of patients with unilateral and bilateral full DBS systems operated for DBS surgery at Albany Medical Center. Examples of 3D-rendered view of post-operation CT images of two patients are also shown

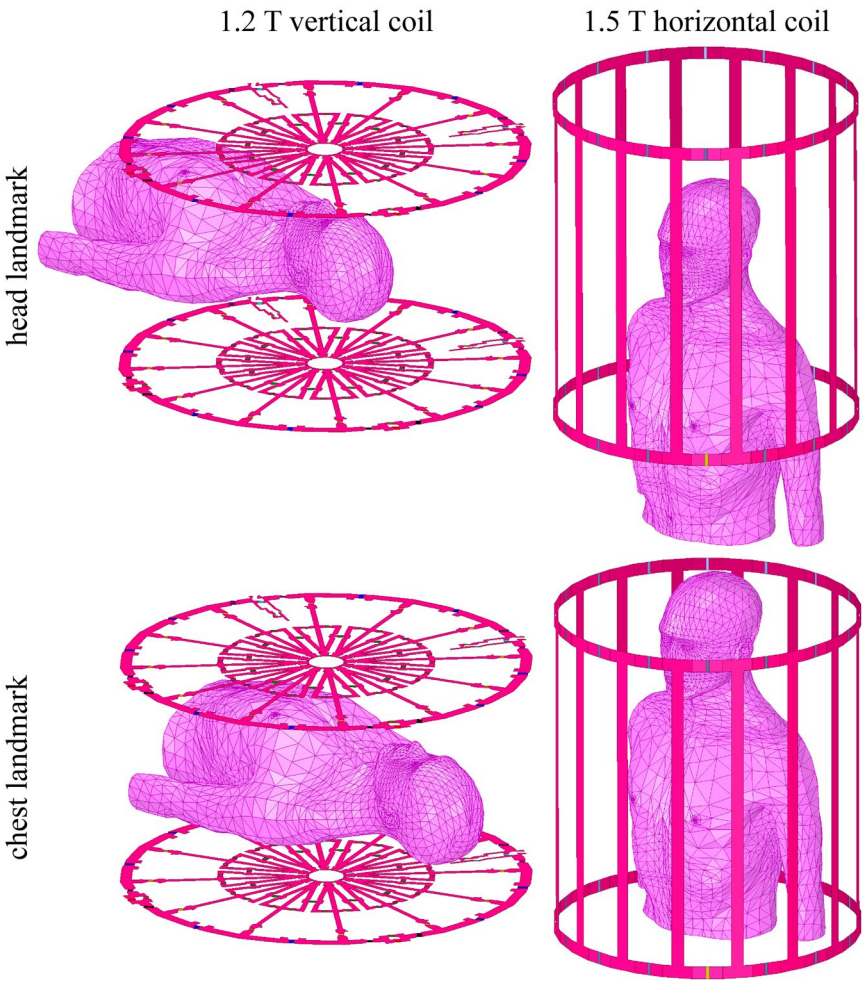

FIGURE 4 The 1.2T vertical OASIS coil and 1.5T horizontal birdcage coil arrangement with a human body model positioned in two different (head and chest) imaging landmarks

of relying only on HFSS convergence criteria, which is based on the S-parameters.

2.2 | Experiments

RF heating experiments were performed using an anthropomorphic phantom consisting of a human-shaped head and torso and a 3D-printed skull structure similar to what was used in our previous work.[31] In brief, CT images of a patient with deep brain stimulation implants were used to segment patient's silhouette and skull in 3D Slicer (Slicer 4.10, http://slicer.org) and segmented masks were processed in a CAD tool (Rhino 6.0, Robert McNeal & Associates, Seattle, WA) to create watertight models of the skull, head, and torso. The skull structure was designed to split into two halves along the coronal plane so that it could be opened and refilled with different brain-mimicking materials. All parts were 3D-printed in ABS plastic and coated with acrylic for waterproofing. Tissue mimicking gel was prepared by mixing 32 g/L of edible agar (Landor Trading Company, gel strength 900 g/cm^2) with saline solution (2.25 gNaCL/L) while heating with continuous stirring until a uniform solution was formed. The solution was allowed to cool down to 60 ℃ and poured into the skull to solidify. The thermal conductivity of agar gel has been reported to be near 0.56 J/k-S at concentrations in the range of 10 g/L to 50 g/L.[32] The conductivity at our concentration (32g/L) was, therefore, close to 0.56 J/K-S, similar to that of brain gray matter (0.55 J/k-S).[33] The semi-solid gel had a viscosity close to the tissue which prevented convective heat transfer, allowing conservative heat measurements. The gel, however, did not account for the perfusion and, thus, measured temperatures represented the upper limit of what happens *in-vivo*. Electric conductivity and relative permittivity of the solidified gel was measured using a vector network analyzer (Keysight technologies, Santa Rosa, CA) to be $\sigma = 0.4$ S/m and $\varepsilon_r = 78$. The body of the phantom was filled with 18 L of saline solution ($\sigma = 0.48$ S/m and $\varepsilon_r = 78$).

Experiments were performed with both insulated wires (diameter = 0.65 mm, insulation thickness = 0.35 mm) and a commercial DBS system. We used 40 cm wires representing lead only systems and 100 cm wires representing full DBS systems (lead + extension). Wires were exposed at the tip (2 mm) and attached to a fluoroptic temperature

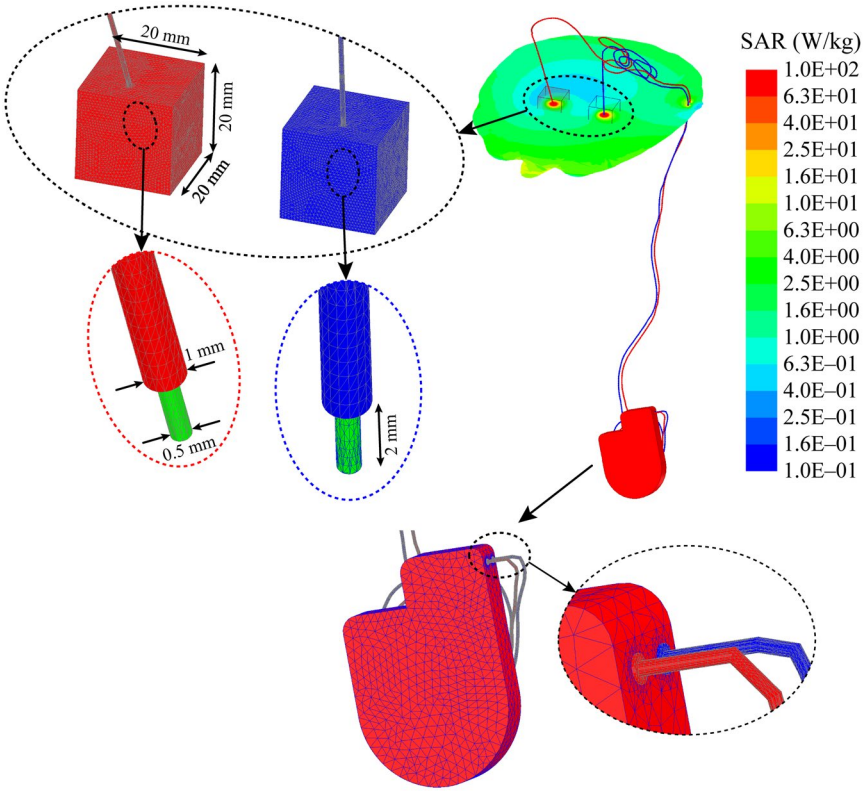

FIGURE 5 Example of mesh distribution in the lead, insulation, SAR boxes, and IPG. The distribution of 0.1 g-SAR in a plane passing through the lead tip has also been shown for a patient with full DBS system (1.5T horizontal birdcage coil / head landmark / ID47)

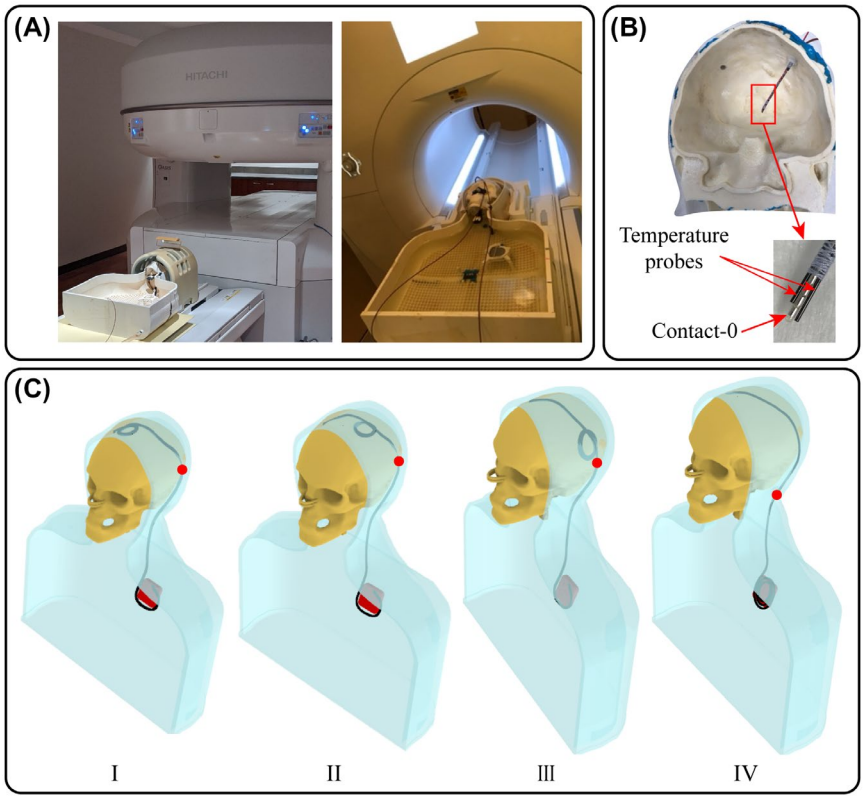

FIGURE 6 Phantom and experimental setup. A, Anthropomorphic phantom in the 1.2T vertical scanner (left) and a 1.5T horizontal scanner (right). B, DBS lead attached to temperature probes implanted into the skull. C, Schematic of phantom setup showing different trajectories (I, II, III, and IV) with different loop positions. The red dot represents the 40 cm mark measured from the intracranial end, representing the end-point for 40 cm wire

probe (OSENSA, BC, Canada) at the exposed tip using a string. Experiments with a full DBS system were performed using a Medtronic system (Medtronic Inc., Minneapolis, MN) using a 40 cm lead (model 3389), 60 cm extension (model 3708660) and implantable pulse generator (Activa SC −37603). Temperature probes were attached to the most distal contact (contact 0) and contact 1 of the DBS lead (see Figure 6B). Lead and wires were inserted into the skull

following the entry point and the angle of penetration similar to that of surgical implantation approach for targeting STN.

For each implant (40 cm wire, 100 cm wire, and Medtronic DBS system), the extracranial portion of the lead/wire was routed along four different trajectories as depicted in Figure 6C. Trajectory I consisted of two concentric loops at the surgical burr hole, with the rest of wire/lead routed medio-laterally toward the neck and the excess length of wire/extension looped around the IPG as recommended in the manufacturer's clinician manual. This configuration has been shown to minimize RF heating of fully implanted DBS devices at 3 T,[29] and is implemented as the standard of care surgical approach by some groups.[34] Trajectory II consisted of two concentric loops moved farther from the surgical burr hole along the coronal suture, which is a common lead arrangement observed on post-operative CT images. Trajectory III consisted of two loops above the temporal bone, with the rest of extension/wire routed similar to previous two cases. This lead configuration is shown to reduce RF heating of fully implanted DBS devices at 1.5T[29] and is implemented by some groups to reduce the susceptibility artifact above the motor cortex that contaminates fMRI signal.[35] Finally, trajectory IV had no loop on the skull with all excess length of the lead + extension looped around the IPG. This trajectory has been shown to generate maximum RF heating at both 1.5T and 3T horizontal scanners.[29]

RF heating measurements were performed at a Siemens 1.5T Aera scanner (Siemens Healthineers, Erlangen, Germany) and a Hitachi 1.2T Oasis vertical scanner (Hitachi Healthcare) using high SAR turbo spin echo (TSE) sequences with parameters given in Table 1. Sequence parameters were adjusted to produce rms B_1^+ of 4μT at both scanners. Because the total acquisition time (TA) at 1.5T was slightly longer than at 1.2T (4 min 14 s vs. 3 min 22 s), comparisons between Δ*T*s were made after 3 min 22 s for both scanners. The position and size of loops were kept identical between the experiments at two scanners by marking lead routes on the skull as well as on the implanted leads.

TABLE 1 Sequence parameters for the sequences used for RF heating measurements at 1.5T horizontal scanner and 1.2T vertical scanner

Sequence Parameters	T1-TSE at 1.5T Aera	T2-FSE at 1.2T Oasis
Echo time	7.3	96
TR	814	2728
FA	150	90
Matrix size	192 × 192	512 × 320
TA	4:14	3:22
B_1^+ rms (μT)	4	4
Number of averages	2	2

3 | RESULTS

3.1 | SAR calculations

Figure 7 shows an example of 0.1 g-SAR distribution (patient #47) on an axial plane passing through the electrodes. Compared to the 1.5T horizontal birdcage, OASIS coil generated ~57-fold and 75-fold less SAR around lead tips at head and chest imaging landmarks, respectively. Similarly, compared to the horizontal birdcage tuned to 1.2T, OASIS coil generated 81-fold and 64-fold less SAR around lead tips at head and chest imaging landmarks, respectively. Supporting Information Video S1 also demonstrates the time evolution of incident **E** field vector as well as the tangential component of incident **E** field along trajectories of the leads in patient #47 for the 1.2T vertical OASIS coil and 1.2T and 1.5T horizontal birdcage coils. These simulations were performed without the implants to generate the incident field, but field values are visualized along hypothetical lead trajectories. The coil's input power was adjusted for all simulations to generate a mean $B_1^+ = 4\mu T$ over a circular plane placed on an axial plane passing through the coil's iso-center. We observed that the orientation of the incident electric field of the vertical coil was mostly orthogonal to the trajectory of DBS leads (ie, smaller tangential component), a criterion that is demonstrated to predict lower RF heating in previous studies[10] and also according to the well-established concept of lead's transfer function.[36]

Figure 8 depicts the box plot of the 0.1 g-SAR_{max} over all 90 lead models for the 1.2T vertical OASIS coil, as well as 1.2T and 1.5T horizontal birdcage coils at head and chest imaging landmarks. The mean, median, SD, and interquartile range (IQR) of the 0.1 g-SARmax are also given in Supporting Information Table S2. The outliers were plotted individually as red "+" symbols. For the head landmark, the mean ± SD of 0.1 g-SAR_{max} was 17 ± 26.8 W/kg for the 1.2T OASIS coil and 519.3 ± 694.6 W/kg for the 1.5T horizontal birdcage coil. At the chest landmark, the mean ± SD of 0.1 g-SAR_{max} was 10.2 ± 35.5 W/kg for the 1.2T OASIS coil and 268.3 ± 671.5 W/kg for the 1.5T horizontal birdcage coil. For the 1.2T horizontal birdcage coil, the mean ± SD of 0.1 g-SAR_{max} was 608.9 ± 1077.1 W/kg and 411.2 ± 836.9 W/kg at the head and chest landmarks, respectively.

A paired one-tailed t-test showed a significant reduction in SAR generated by the 1.2T vertical coil compared to 1.5T horizontal coil at head landmark ($P < 1 \times 10^{-5}$, Cohen's d = 0.73) as well as chest imaging landmark ($P < 1.9 \times 10^{-4}$, Cohen's d = 0.4). Similarly, there was a significant reduction in SAR generated by the 1.2T Oasis vertical coil compared to 1.2T horizontal birdcage coil during imaging at head landmark ($P < 1.7 \times 10^{-4}$, Cohen′s d = 0.55) as well as chest imaging landmark ($P < 7 \times 10^{-4}$, Cohen's d = 0.49).

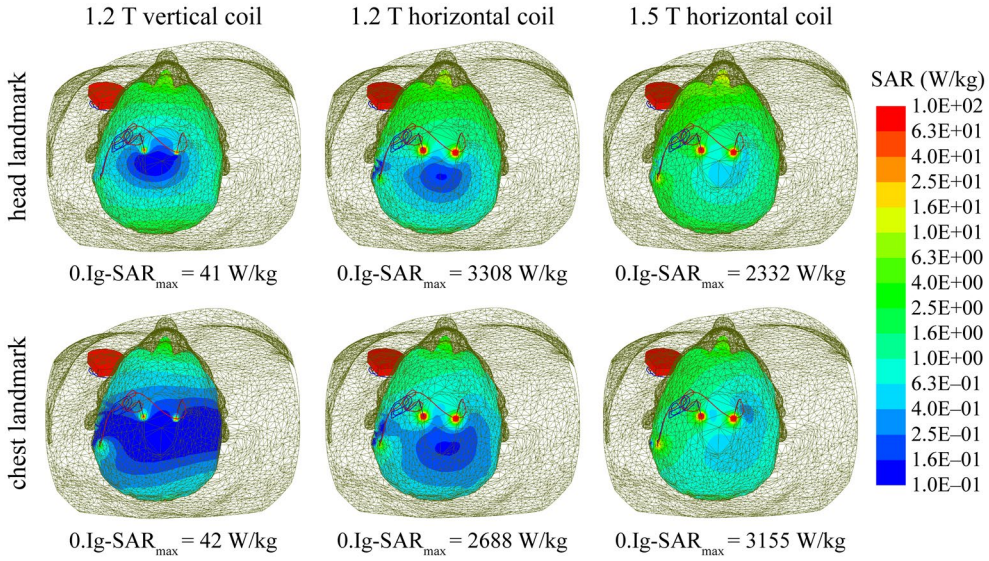

FIGURE 7 Distributions of 0.1 g-SAR in patient 47 (ID47) for the 1.2T OASIS coil and 1.2T and 1.5T horizontal birdcage coils, all with head and chest imaging landmarks, on an axial plane that passes through the tips of implants. In all maps, the coil's input power is adjusted to generate a mean $B_1^+ = 4$ μT over a circular plane placed on an axial plane passing through the coil's iso-center

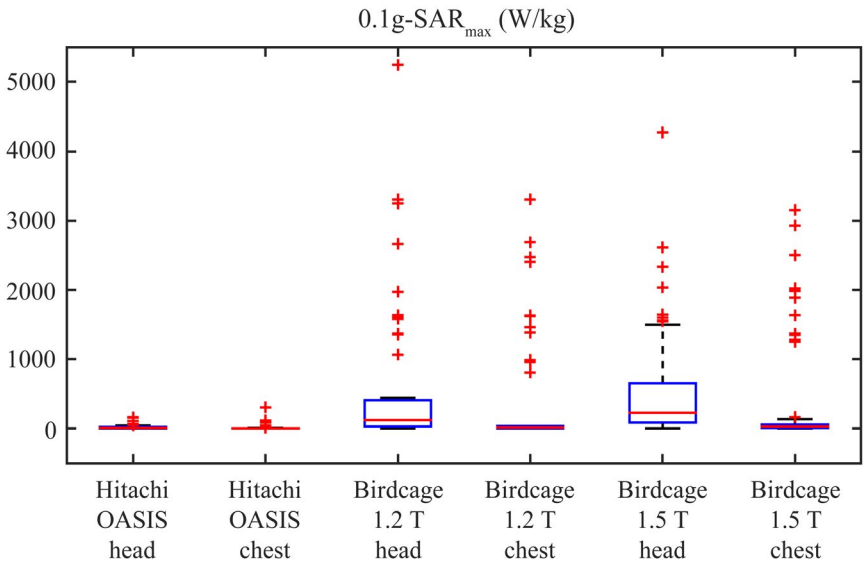

FIGURE 8 Box plot of 0.1 g-SAR$_{max}$ for different trajectories with different transmit coil systems and using different imaging landmarks (head and chest)

Additionally, imaging at head landmark generated significantly larger SAR compared to chest imaging landmark for all coils ($P < 0.005$, Cohen's d = 0.28, for 1.2T vertical coil; $P < 4.3 \times 10^{-5}$, Cohen's d = 0.61 for 1.2T horizontal birdcage coil; $P < 1 \times 10^{-5}$, Cohen's d = 0.65 for 1.5T horizontal birdcage coil).

3.2 | RF heating measurements

The temperature rise measured at the lead tip for each implant configuration during MRI scanning at both 1.5T horizontal scanner and 1.2T vertical scanner is given in Figure 9. The plots show that for most of the cases the temperature increase was substantially higher at 1.5T horizontal scanner compared to 1.2T vertical scanner. (The numerical values of temperature rise are presented in the Supporting Information Table S3.) The mean ± SD of temperature increase was 5.21 ± 7.22 °C for the 1.5T horizontal scanner and 0.58 ± 0.27 °C for the 1.2T vertical scanner, indicating an approximately nine-fold reduction in mean temperature rise using vertical scanner. For the cases evaluated during the RF heating measurements, the worst-case heating at 1.5T horizontal scanner was ~21-fold higher than the worst-case heating at 1.2T vertical scanner (25.85 °C vs 1.24 °C). Also, a one tailed paired t-test showed a significant reduction in heating at 1.2T vertical scanner compared to 1.5T horizontal scanner ($P < 0.026$, Cohen's d = 0.63).

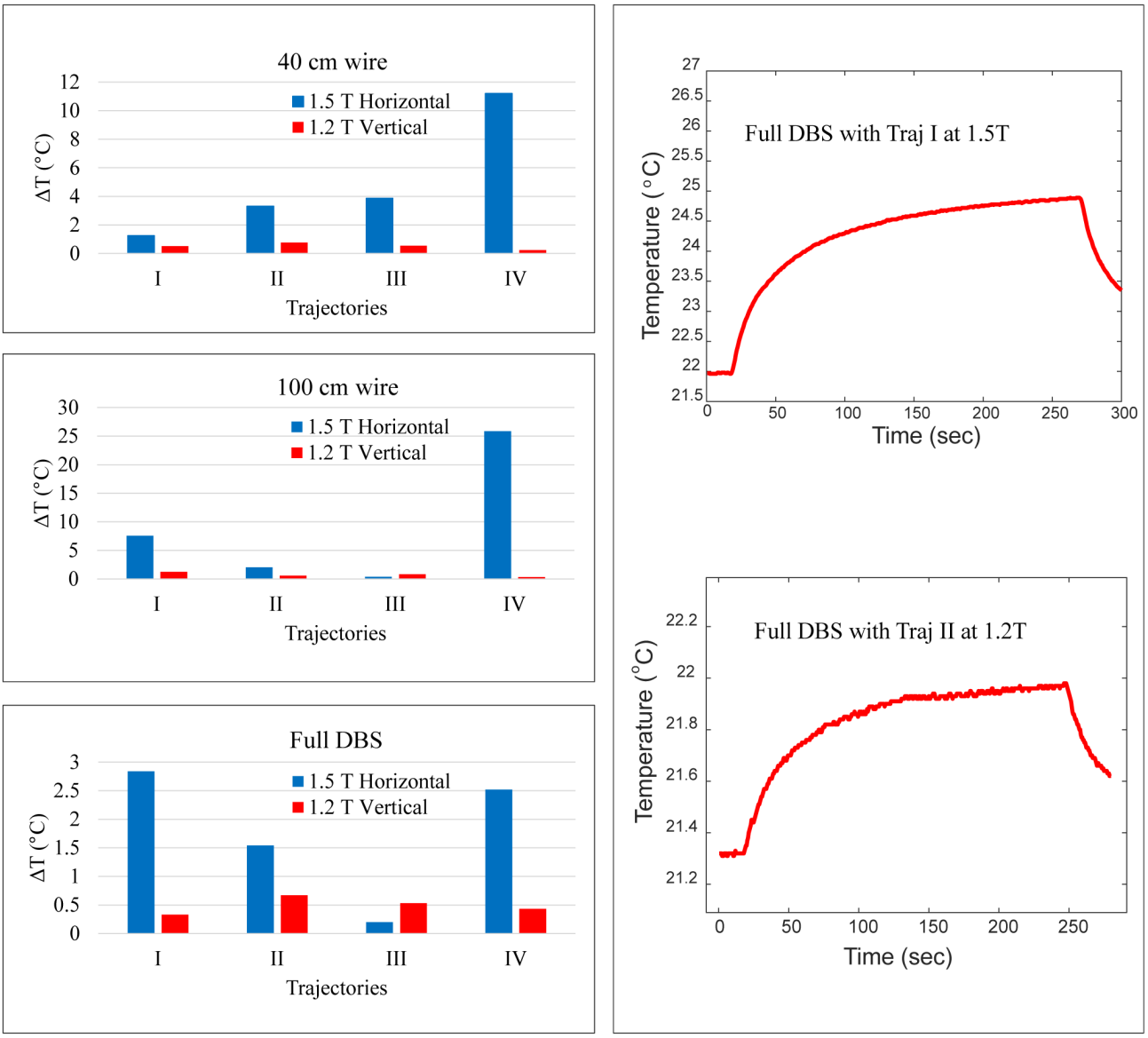

FIGURE 9 Plots of measured temperature increase at the lead tip for each implant model (40 cm wire, 100 cm wire, and full DBS system), each having four trajectory configurations of extra-cranial lead (trajectories I, II, III, and IV) as depicted in Figure 6. Additionally, the variation of temperature at the DBS electrode with time is presented for the cases with the highest temperature rise for the full DBS system observed at 1.5T horizontal scanner (trajectory I) and 1.2T vertical scanner (trajectory II)

4 | DISCUSSION AND CONCLUSIONS

The market size of active implantable medical devices is estimated to grow at an annual rate of 7.8% to reach ~$27 Billion by 2022.[37] Factors driving such steep growth include an aging population, increased prevalence of cardiovascular and neurological diseases, advancements in implantable device technology, and favorable reimbursement policies in developed countries, to name a few. MRI is the imaging modality of choice for the majority of neurologic, cardiac, and musculoskeletal disorders. It is estimated that 50%-75% of patients with cardiovascular implants will need to undergo MRI during their lifetime,[38] with many patients requiring repeated examinations.[39] Similarly, MRI is increasingly indicated in patients with neuro-modulation devices, such as those with DBS implants,[40] as it can directly visualize implanted electrodes,[41,42] and allow the stimulation to be tailored on a patient-specific basis to maximize the therapy and minimize side effects.[41-44] Indeed, lessons learned from failed clinical trials have brought the consensus that meticulous application of neuroimaging is indispensable to guide neuro-modulation therapies, both for target verification and ruling out complications, and for quantifying the functional effects of stimulation on sparse brain networks across participants and etiologies.[45,46]

The past few years have witnessed a spike in engineering efforts to realize implant-friendly MRI. Pioneering

work has been done to advance MRI field-shaping methods, techniques that manipulate the electric field of MRI transmit coil to eliminate its interaction with individual patient's implants.[2,9,26,47-52] Another alternative approach is surgical device management, where trajectories of implanted leads are surgically modified (based on computer simulations) such that their coupling with MRI electric fields is minimized.[8,10,29] Finally, there has been a spate of patents proposing novel implant structures[53-57] and materials[11,58] to reduce induced RF currents, and by proxy, RF heating. These efforts, however, have been mostly focused on closed-bore scanners with conventional horizontal (solenoidal) birdcage transmit coils. Vertical scanners, originally introduced as open-bore low-field MRI, have 90° rotated magnetic fields which in turn generates a fundamentally different distribution of RF fields inside the body.[59] As the RF heating of an elongated implant is highly sensitive to the orientation of implant's trajectory with respect to MRI electric fields,[36,60] it is theoretically conceivable that vertical scanners generate a significantly different RF heating around implanted leads compared to conventional scanners.

In an earlier work, we simulated the SAR at tips of three DBS lead models and showed that for the same magnitude of B_1^+, local SAR was substantially reduced in a vertical 1.2T scanner coil compared with a birdcage at 1.5T horizontal (solenoidal) scanner.[11] This contribution expanded the previous work to a cohort of 90 patient-derived lead models, including both lead-only and fully implanted devices. We focused on DBS implants, as their RF heating has substantial safety ramifications considering the sensitivity of the organ at risk (brain). Because RF heating depends on lead's trajectory, and because there is a considerable patient-to-patient variation in routing trajectories of DBS leads depending on surgeon's practice style,[61] we recruited patients from two DBS centers operated by different neurosurgeons. Our results showed that for the same magnitude of B_1^+ at the coil's iso-center, the mean of 0.1 g-SAR_{max} around implanted leads generated by a vertical 1.2T butterfly coil was reduced by ~30-fold compared to the birdcage coil at 1.5T and that this SAR reduction was statistically significant ($P < 1 \times 10^{-5}$). Interestingly, the 1.2T butterfly coil significantly reduced the SAR compared to the 1.2T birdcage coil (~35-fold, $P < 1.7 \times 10^{-4}$), indicating that the SAR reduction performance was mostly attributable to the change in the orientation of the electric field rather than changes in resonance frequency.

This work also provides the first experimental results of RF heating of a commercial DBS device in a 1.2T vertical scanner (OASIS, Hitachi) compared to a 1.5T horizontal scanner (Aera, Siemens). Although our simulations were performed with a homogeneous body model, the phantom used in experiments was composed of three different materials representing properties of bone ($\sigma \cong 0$), brain tissue ($\sigma = 0.4$ S/m), and average body tissue ($\sigma = 0.48$ S/m). This phantom has been shown to predict a similar trend of RF heating of DBS devices as in a heterogeneous body model.[30] RF heating was reduced by an average of approximately nine-fold in the 1.2T vertical coil compared to the 1.5T horizontal coil and the reduction was significant ($P < .026$). As the gradients were on during all measurements, the reported temperature rises theoretically reflect the combined effect of gradient-induced heating and RF-induced heating. However, it should be noted that although gradient-induced heating can reach non-trivial levels in bulk conductors,[62] its effect is negligible for the case of elongated leads as noted in Section 9 of ISO-TS10974.[63]

The measured temperature increase varied substantially (order of magnitude) among different trajectories during MRI at 1.5T, consistent with the previously reported studies.[10,29] However, the temperature increase varied less during MRI at 1.2T vertical scanner and was below 2°C for all configurations evaluated in this study. For the full DBS system as well as the 100 cm wire when routed along trajectory III, the temperature increase was higher at 1.2T compared to that at 1.5T, although the values were less than 1°C for each scanner. This trajectory has been shown to minimize RF heating at 1.5T horizontal scanner.[29,30] For the commercial DBS device, the worst-case RF heating was reduced from ~3°C to <0.4°C, allowing non-restricted application of MRI imaging. This work is the first to provide strong evidence of a significantly reduced RF heating of DBS leads in a 1.2T OASIS scanner compared to a 1.5T conventional system. The results indicate new possibilities for scanning of patients with electronically active implants.

ACKNOWLEDGMENTS

This work was supported by the NIH grant R03EB025344 and a grant from Hitachi Healthcare Americas.

ORCID

Ehsan Kazemivalipour https://orcid.org/0000-0003-4221-2397
Bhumi Bhusal https://orcid.org/0000-0002-4404-9784
Jasmine Vu https://orcid.org/0000-0001-6288-1446
Ergin Atalar https://orcid.org/0000-0002-6874-6103

REFERENCES

1. Rezai AR, Finelli D, Nyenhuis JA, et al. Neurostimulation systems for deep brain stimulation: in vitro evaluation of magnetic resonance imaging–related heating at 1.5 Tesla. *J Magn Reson Imaging*. 2002;15:241-250.
2. McElcheran CE, Yang B, Anderson KJT, et al. Parallel radiofrequency transmission at 3 Tesla to improve safety in bilateral implanted wires in a heterogeneous model. *Magn Reson Med*. 2017;78:2406-2415.

3. Medical SJ. *MRI Procedure Information*; 2018. https://manuals.sjm.com/~/media/manuals/product-manual-pdfs/d/6/d6db9679-aaa7-4e22-b1e3-1d8a2ac43b98.pdf. Accessed April 20, 2021.
4. Schäfer A, Forstmann BU, Neumann J, et al. Direct visualization of the subthalamic nucleus and its iron distribution using high-resolution susceptibility mapping. *Hum Brain Mapp*. 2012;33:2831-2842.
5. Slavin K, Thulborn K, Wess C, et al. Direct visualization of the human subthalamic nucleus with 3T MR imaging. *Am J Neuroradiol*. 2006;27:80-84.
6. Sudhyadhom A, Haq IU, Foote KD, et al. A high resolution and high contrast MRI for differentiation of subcortical structures for DBS targeting: the fast gray matter acquisition T1 inversion recovery (FGATIR). *Neuroimage*. 2009;47:T44-T52.
7. Yeung CJ, Susil RC, Atalar E. RF heating due to conductive wires during MRI depends on the phase distribution of the transmit field. *Magn Reson Med*. 2002;48:1096-1098.
8. Golestanirad L, Angelone LM, Iacono MI, et al. Local SAR near deep brain stimulation (DBS) electrodes at 64 and 127 MH z: a simulation study of the effect of extracranial loops. *Magn Reson Med*. 2017;78:1558-1565.
9. Golestanirad L, Keil B, Angelone LM, et al. Feasibility of using linearly polarized rotating birdcage transmitters and close-fitting receive arrays in MRI to reduce SAR in the vicinity of deep brain simulation implants. *Magn Reson Med*. 2017;77:1701-1712.
10. Golestanirad L, Kirsch J, Bonmassar G, et al. RF-induced heating in tissue near bilateral DBS implants during MRI at 1.5 T and 3T: The role of surgical lead management. *Neuroimage*. 2019;184:566-576.
11. Golestanirad L, Angelone LM, Kirsch J, et al. Reducing RF-induced heating near implanted leads through high-dielectric capacitive bleeding of current (CBLOC). *IEEE Trans Microw Theory Tech*. 2019;67:1265-1273.
12. Kazemivalipour E, Vu J, Lin S, et al. RF heating of deep brain stimulation implants during MRI in 1.2 T vertical scanners versus 1.5 T horizontal systems: a simulation study with realistic lead configurations. 2020 42nd Annual International Conference of the IEEE Engineering in Medicine & Biology Society (EMBC): IEEE. 2020, pp. 6143-6146.
13. Ibrahim T, Lee R, Baertlein B, et al. B1 field homogeneity and SAR calculations for the birdcage coil. *Phys Med Biol*. 2001;46:609.
14. Ibrahim TS, Lee R, Baertlein BA, et al. Computational analysis of the high pass birdcage resonator: finite difference time domain simulations for high-field MRI. *Magn Reson Imaging*. 2000;18:835-843.
15. Collins CM, Liu W, Wang J, et al. Temperature and SAR calculations for a human head within volume and surface coils at 64 and 300 MHz. *J Magn Reson Imaging*. 2004;19:650-656.
16. Collins CM, Li S, Smith MB. SAR and B1 field distributions in a heterogeneous human head model within a birdcage coil. *Magn Reson Med*. 1998;40:847-856.
17. Lucano E, Liberti M, Mendoza GG, et al. Assessing the electromagnetic fields generated by a radiofrequency MRI body coil at 64 mhz: defeaturing versus accuracy. *IEEE Trans Biomed Eng*. 2015;63:1591-1601.
18. Wolf S, Diehl D, Gebhardt M, et al. SAR simulations for high-field MRI: how much detail, effort, and accuracy is needed? *Magn Reson Med*. 2013;69:1157-1168.
19. Fujimoto K, Zaidi TA, Lampman D, et al. Specific absorption rate (SAR) comparison in the conventional and open MRI systems utilizing an anatomical human computational model. *Proc Intl Soc Mag Reson Med*. 2021;28:1616.
20. Ochi H, Soutome Y, Bito Y, Suzuki S, Shimoda T, Taniguchi T. High frequency coil for magnetic resonance imaging device. Patent Number WO/2008/108048. December 9, 2008.
21. Yeo DT, Wang Z, Loew W, et al. Local SAR in high pass birdcage and TEM body coils for multiple human body models in clinical landmark positions at 3T. *J Magn Reson Imaging*. 2011;33:1209.
22. Yeung CJ, Susil RC, Atalar E. RF safety of wires in interventional MRI: using a safety index. *Magn Reson Med*. 2001;47:187-193.
23. Nguyen BT, Pilitsis J, Golestanirad L. The effect of simulation strategies on prediction of power deposition in the tissue around electronic implants during magnetic resonance imaging. *Phys Med Biol*. 2020;65:185007.
24. Golestanirad L, Rahsepar AA, Kirsch JE, et al. Changes in the specific absorption rate (SAR) of radiofrequency energy in patients with retained cardiac leads during MRI at 1.5 T and 3T. *Magn Reson Med*. 2019;81:653-669.
25. Nordbeck P, Weiss I, Ehses P, et al. Measuring RF-induced currents inside implants: impact of device configuration on MRI safety of cardiac pacemaker leads. *Magn Reson Med*. 2009;61:570-578.
26. Golestanirad L, Kazemivalipour E, Keil B, et al. Reconfigurable MRI coil technology can substantially reduce RF heating of deep brain stimulation implants: first in-vitro study of RF heating reduction in bilateral DBS leads at 1.5 T. *PLoS One*. 2019;14:e0220043.
27. Vu J, Bhusal B, Nguyen BT, et al. Evaluating accuracy of numerical simulations in predicting heating of wire implants during MRI at 1.5 T. 2020 42nd Annual International Conference of the IEEE Engineering in Medicine & Biology Society (EMBC): IEEE. 2020, pp. 6107-6110.
28. Nordbeck P, Ritter O, Weiss I, et al. Impact of imaging landmark on the risk of MRI-related heating near implanted medical devices like cardiac pacemaker leads. *Magn Reson Med*. 2011;65:44-50.
29. Bhusal B, Nguyen BT, Sanpitak P, et al. Effect of device configuration and patient's body composition on the RF heating and non-susceptibility artifact of deep brain stimulation implants during MRI at 1.5 T and 3 T. *J Magn Reson Imaging*. 2020;53:599-610.
30. Bhusal B, Keil B, Rosenow J, et al. Patient's body composition can significantly affect RF power deposition in the tissue around DBS implants: ramifications for lead management strategies and MRI field-shaping techniques. *Phys Med Biol*. 2021;66:015008.
31. Bhusal B, Nguyen BT, Vu J, et al. Device configuration and patient's body composition significantly affect RF heating of deep brain stimulation implants during MRI: an experimental study at 1.5 T and 3T. 2020 42nd Annual International Conference of the IEEE Engineering in Medicine & Biology Society (EMBC): IEEE. 2020, pp. 5192-5197.
32. Zhang M, Che Z, Chen J, et al. Experimental determination of thermal conductivity of water– agar gel at different concentrations and temperatures. *J Chem Eng Data*. 2011;56:859-864.
33. IT'IS Foundation. Thermal Conductivity. https://itis.swiss/virtual-population/tissue-properties/database/thermal-conductivity/. Accessed April 20, 2021.
34. Davidson B, Tam F, Yang B, et al. Three-Tesla magnetic resonance imaging of patients with deep brain stimulators: results from a phantom study and a pilot study in patients. *Neurosurgery*. 2021;88:349-355.
35. Boutet A, Rashid T, Hancu I, et al. Functional MRI safety and artifacts during deep brain stimulation: experience in 102 patients. *Radiology*. 2019;293:174-183.

36. Park SM, Kamondetdacha R, Nyenhuis JA. Calculation of MRI-induced heating of an implanted medical lead wire with an electric field transfer function. *J Magn Reson Imaging*. 2007;26:1278-1285.
37. *Neurostimulatin devices: Market estimation & trend analysis from 2016 to 2024*. San Francisco, CA: Grand View Research, Inc; 2016.
38. Kalin R, Stanton MS. Current clinical issues for MRI scanning of pacemaker and defibrillator patients. *Pacing Clin Electrophysiol*. 2005;28:326-328.
39. Naehle CP, Zeijlemaker V, Thomas D, et al. Evaluation of cumulative effects of MR imaging on pacemaker systems at 1.5 Tesla. *Pacing Clin Electrophysiol*. 2009;32:1526-1535.
40. Falowski S, Safriel Y, Ryan MP, et al. The rate of magnetic resonance imaging in patients with deep brain stimulation. *Stereotact Funct Neurosurg*. 2016;94:147-153.
41. Cui Z, Pan L, Song H, et al. Intraoperative MRI for optimizing electrode placement for deep brain stimulation of the subthalamic nucleus in Parkinson disease. *J Neurosurg*. 2016;124:62-69.
42. Ramani S, Schulte R, Mckinnon G, et al. Accurate localization of individual DBS contacts by MRI using zero-TE phase images. *Proc Intl Soc Mag Reson Med*. 2018;26:2687.
43. DiMarzio M, Madhavan R, Joel S, et al. Use of functional magnetic resonance imaging to assess how motor phenotypes of Parkinson's disease respond to deep brain stimulation. *Neuromodulation: Technology at the Neural Interface*. 2020;23:515-524.
44. DiMarzio M, Rashid T, Hancu I, et al. Functional MRI signature of chronic pain relief from deep brain stimulation in Parkinson disease patients. *Neurosurgery*. 2019;85:E1043-E1049.
45. Lozano AM, Lipsman N, Bergman H, et al. Deep brain stimulation: current challenges and future directions. *Nat Rev Neurol*. 2019;15:148-160.
46. Horn A. The impact of modern-day neuroimaging on the field of deep brain stimulation. *Curr Opin Neurol*. 2019;32:511-520.
47. Golestanirad L, Iacono MI, Keil B, et al. Construction and modeling of a reconfigurable MRI coil for lowering SAR in patients with deep brain stimulation implants. *Neuroimage*. 2017;147:577-588.
48. Kazemivalipour E, Keil B, Vali A, et al. Reconfigurable MRI technology for low-SAR imaging of deep brain stimulation at 3T: application in bilateral leads, fully-implanted systems, and surgically modified lead trajectories. *Neuroimage*. 2019;199:18-29.
49. McElcheran CE, Golestanirad L, Iacono MI, et al. Numerical simulations of realistic lead trajectories and an experimental verification support the efficacy of parallel radiofrequency transmission to reduce heating of deep brain stimulation implants during MRI. *Sci Rep*. 2019;9:1-14.
50. McElcheran CE, Yang B, Anderson KJT, et al. Investigation of parallel radiofrequency transmission for the reduction of heating in long conductive leads in 3 Tesla magnetic resonance imaging. *PLoS One*. 2015;10:e0134379.
51. Eryaman Y, Guerin B, Akgun C, et al. Parallel transmit pulse design for patients with deep brain stimulation implants. *Magn Reson Med*. 2014;73:1896-1903.
52. Eryaman Y, Kobayashi N, Moen S, et al. A simple geometric analysis method for measuring and mitigating RF induced currents on deep brain stimulation leads by multichannel transmission/reception. *Neuroimage*. 2019;184:658-668.
53. Olsen JM, Hrdlicka GA, Wahlstrand CD, et al. Lead Electrode for Use in an MRI-Safe Implantable Medical Device. US Patent US7877150B2. 2010.
54. McCabe S, Scott J. A novel implant electrode design safe in the RF field of MRI scanners. *IEEE Trans Microw Theory Tech*. 2017;65:3541-3547.
55. Stevenson RA, Halperin HR, Lardo AC, et al. Implantable Lead Bandstop Filter Employing an Inductive Coil with Parasitic Capacitance to Enhance MRI Compatibility of Active Medical Devices. US Patent US8903505B2. 2012.
56. Atalar E, Allen J, Bottomley P et al. MRI-Safe High Impedance Lead Systems. US Patent US8055351B2. 2011.
57. Vase A, Sethna DN. Implantable Medical Lead Configured for Improved MRI Safety. US Patent US20090270956A1. 2008.
58. Serano P, Angelone LM, Katnani H, et al. A novel brain stimulation technology provides compatibility with MRI. *Sci Rep*. 2015;5:1-10.
59. Kakugawa S, Kitamura S, Hara N, et al. Open MRI System with a Vertical Static Field and an Imaging Volume Closer to the Lower Than to the Upper Magnet Assembly. US Patent US6600318B1. 2003. https://patentimages.storage.googleapis.com/cc/39/e1/ab1cf9f453ca41/US6600318.pdf. Accessed April 20, 2021.
60. Yeung CJ, Susil RC, Atalar E. RF heating due to conductive wires during MRI depends on the phase distribution of the transmit field. *Magn Reson Med*. 2002;48:1096-1098.
61. Golestanirad L, Pilitsis J, Martin A, et al. Variation of RF heating around deep brain stimulation leads during 3.0 T MRI in fourteen patient-derived realistic lead models: the role of extracranial lead management. *Proc Intl Soc Mag Reson Med*. 2017;25:0484.
62. Brühl R, Ihlenfeld A, Ittermann B. Gradient heating of bulk metallic implants can be a safety concern in MRI. *Magn Reson Med*. 2017;77:1739-1740.
63. ISO/TS 10974:2018. *Assessment of the Safety of Magnetic Resonance Imaging for Patients with an Active Implantable Medical Device*. Geneva, Switzerland: International Organization for Standardization; 2018.

SUPPORTING INFORMATION

Additional Supporting Information may be found online in the Supporting Information section.

TABLE S1 Maximum of 0.1g SAR values for patient 47 (ID47) with different convergence thresholds

TABLE S2 Maximum of 0.1g SAR

TABLE S3 Measured temperature increase at the lead tip for each implant model

VIDEO S1 Incident **E** field (arrows) and $\mathbf{E}_{tan}$ (color field overlaid on leads) for varying intrinsic phases along lead trajectories in patient #47 for the 1.2 T vertical OASIS coil and 1.2 T and 1.5 T horizontal birdcage coils. Simulations were done for the head imaging landmark and the coil's input power was adjusted to generate a mean $B_1^+ = 4$ μT over a circular plane placed on an axial plane passing through the coil's iso-center

How to cite this article: Kazemivalipour E, Bhusal B, Vu J, et al. Vertical open-bore MRI scanners generate significantly less radiofrequency heating around implanted leads: A study of deep brain stimulation implants in 1.2T OASIS scanners versus 1.5T horizontal systems. *Magn Reson Med*. 2021;86:1560–1572. https://doi.org/10.1002/mrm.28818